RSC Advances

PAPER

View Article Online
View Journal | View Issue

Cite this: *RSC Adv.*, 2019, **9**, 9171

Facile preparation of amidoxime-functionalized $Fe_3O_4@SiO_2$-*g*-PAMAM-AO magnetic composites for enhanced adsorption of Pb(II) and Ni(II) from aqueous solution

Dai Yimin,* Liu Danyang, Zou Jiaqi, Wang Shengyun and Zhou Yi

Received 7th January 2019
Accepted 2nd March 2019

DOI: 10.1039/c9ra00128j

rsc.li/rsc-advances

In this paper, using amidoxime as a functional monomer, different generations of polyamidoxime dendrimer magnetic microspheres ($Fe_3O_4@SiO_2$-*g*-PAMAM-AO) were fabricated to adsorb Pb^{2+} and Ni^{2+} in aqueous solution. The magnetic adsorbents were characterized by FTIR, XRD, SEM, XPS, TEM, EDS, TGA and BET. The effects of different factors (such as solution pH, adsorption time, adsorption temperature, adsorbent dosage *etc.*) on adsorption were evaluated. $Fe_3O_4@SiO_2$-*g*-PAMAM-AO has a maximum Pb(II) adsorption of 157.25 mg g^{-1} (100 mg L^{-1}) at pH 5.5. Furthermore, $Fe_3O_4@SiO_2$-*g*-PAMAM-AO showed an excellent adsorption performance for the removal of Ni(II) with a maximum adsorption capacity of 191.78 mg g^{-1} (100 mg L^{-1}) at pH 8.0. The sorption isotherm data fitted the Freundlich isotherm model well. Adsorption kinetics analysis showed that it was best described by the pseudo-second-order rate model. Desorption experiment results showed that the adsorbent can be reused in the adsorption–desorption cycles.

1. Introduction

Urbanization and industrialization are the biggest cause of toxic heavy metals in the environment, including groundwater, soils, rivers, lakes, and oceans.[1–5] The high toxicity and bio-accumulation of heavy metal ions such as Pb, Ni, Cr, As and Hg in aqueous solution can cause terrible hazards to people.[6–10] Pb(II) and Ni(II) are heavy metal ions that are toxic to the human body because Pb(II), Ni(II) and their compounds will cause harm to many systems such as the nerves, hematopoiesis, kidneys, the cardiovascular system and the endocrine system. When the content is high enough, Pb(II) and Ni(II) poisoning will be caused.[11] Hence, the removal of pollution before discharge into the environment is an urgent matter.

In the past few decades, various methods have been applied to remove heavy metal ions, such as ion exchange,[12] membrane processes,[13] and precipitation.[14] However, the efficiency and economic performance of the removal of heavy metal ions using these techniques are the main obstacles to their practical application. Compared with other methods, the adsorption method is a more attractive method which is cost-effective and highly efficient.[15]

It is well known that amidoxime-functionalized nano-materials have outstanding ability to remove heavy metal ions. The amidoxime-functionalized groups with $-NH_2$ and –OH have the ability of chelation, so the functional groups on the surface of the nanohybrids can form stable chelates with heavy metal ions.[16]

Because different dendrimers have different cavity sizes and end functional groups, target adsorbates can be selectively adsorbed by different kinds of dendrimers.[17,18] Ma *et al.* prepared GO/Fe_3O_4-*g*-PAMAM for the adsorption of Pb(II) in aqueous solution. The adsorption capacity of Pb(II) can be up to 181.4 mg g^{-1} at 30 °C.[19] From their work, the adsorption by GO/Fe_3O_4-*g*-G(3.0) of Pb(II) is obviously higher than that by GO/Fe_3O_4-*g*-PAMAM (G0.5, G1.0, G1.5, G2.0 and G2.5). It was illustrated that the adsorption capacity increased with the increasing generations of PAMAM. However, one disadvantage of GO/Fe_3O_4-*g*-PAMAM is that graphene oxide (GO) has carboxyl and hydroxyl groups, and it can disturb the reaction of maleic anhydride (MAH) and ethanediamine (EDA) and thus reduce the reaction efficiency. Furthermore, these techniques generally suffer from difficult manipulation and high cost as well as long separation time.

To compensate for these disadvantages, taking advantage of the combined benefits of amidoxime and dendrimer, maleic anhydride (MAH) and ethanediamine (EDA) were alternately and repeatedly used to synthesise different generations of dendrimers. Here, we report an amidoxime-functionalized $Fe_3O_4@SiO_2$-*g*-PAMAM-AO magnetic composite for the enhanced ability to adsorb Pb(II) and Ni(II) in aqueous solution. Amidoxime and PAMAM dendrimers grafted into the surface of $Fe_3O_4@SiO_2$ played an important role in preventing the oxidation of Fe_3O_4.[20] In addition, methyl acrylate (MA) and

---

School of Chemistry and Food Engineering, Hunan Provincial Key Laboratory of Materials Protection for Electric Power and Transportation, Changsha University of Science and Technology, Changsha 410114, PR China. E-mail: yimindai@sohu.com

ethanediamine (EDA) were alternated and repeated to increase the generation of dendrimers from the Fe_3O_4 surface. The adsorption capacity increased with the increasing generations of PAMAM. The adsorption characteristics of Fe_3O_4@SiO_2-*g*-PAMAM-AO nanoparticles towards Pb(II) and Ni(II), and the sorption kinetics, sorption capability and regeneration were investigated.

2. Materials and methods

2.1 Materials

Ferric chloride hexahydrate ($FeCl_3 \cdot 6H_2O$), ferrous chloride tetrahydrate ($FeCl_2 \cdot 4H_2O$), sodium hydroxide (NaOH), and ammonia ($NH_3 \cdot H_2O$) were purchased from Xiyu Chemical Reagent Co., Ltd. Polyvinyl pyrrolidone (PVP), methyl acrylate, ethanol, methanol, ethylenediamine, potassium carbonate (K_2CO_3), tetraethyl orthosilicate (TEOS), 3-chloropropyltrimethoxysilane (APTES), hydroxylamine hydrochloride ($NH_2OH \cdot HCl$), glutaraldehyde, and 4-aminobenzonitrile were purchased from Sinopharm Chemical Reagents Co., Ltd. Unless otherwise noted, all chemicals were reagent grade and used without further purification.

2.2 Preparation of Fe_3O_4@SiO_2–NH_2

The magnetic Fe_3O_4 nanoparticles were prepared by the coprecipitation method.[21] A mixture of Fe^{2+} and Fe^{3+} was reacted in distilled water, which was stirred vigorously at 30 °C for 30 minutes. Afterwards, NaOH was added dropwise to keep the pH at 7 and the mixture was continuously reacted for 30 min. Finally, 2 g of PVP was added to the mixture solution and reacted at 50 °C for 2 h; then the temperature was returned to 30 °C. The Fe_3O_4 was filtered with distilled water and ethanol several times to wash it. The Fe_3O_4 was dried at 60 °C for 24 h in a vacuum drying oven.

The modified Stöber method[22] is the classic method to synthesize Fe_3O_4@SiO_2. Firstly, 0.1 g of Fe_3O_4 particles was added to a mixture of water, ethanol and $NH_3 \cdot H_2O$. The ratio of ethanol and water was 4 : 1. Then, 1 ml of TEOS was added to the aqueous solution and kept under stirring at 30 °C for 6 h. The Fe_3O_4@SiO_2 was collected by the method of magnetic separation. The product was washed several times with distilled water and ethanol and then dried at 60 °C for 24 h in a vacuum drying oven. Finally, the Fe_3O_4@SiO_2 was further modified with APTES to obtain Fe_3O_4@SiO_2–NH_2. The Fe_3O_4@SiO_2 was dissolved in a solution of ethanol and water. The ratio of ethanol and water was 4 : 1. The solution was stirred for 10 minutes and $NH_3 \cdot H_2O$ and APTES were added gradually, and the solution was reacted at room temperature for 24 h.

2.3 Preparation of Fe_3O_4@SiO_2-*g*-PAMAM

Firstly, Fe_3O_4@SiO_2–NH_2 was added to methanol in a three-necked flask and ultrasonicated for 10 min. The solution was stirred at 35 °C for 24 h after adding methyl acrylate (MA). This target product was named Fe_3O_4@SiO_2-*g*-G0.5. Secondly, the intermediate product Fe_3O_4@SiO_2-*g*-G0.5 was added to methanol and ultrasonicated for 10 min. And then ethanediamine (EDA) was added dropwise to the mixture and kept under mechanical stirring at 40 °C for 2 h. The target product was named Fe_3O_4@SiO_2-*g*-G1.0. In order to obtain more generations of dendrimers, methyl acrylate (MA) and ethanediamine (EDA) were reacted alternately with the nanocomposites twice, respectively. The products with more generation were prepared using 10% excess volume MA and EDA of the preceding reaction during every step reaction. This experience was reacted four steps and the product Fe_3O_4@SiO_2-*g*-G2.0 was obtained.

2.4 Preparation of Fe_3O_4@SiO_2-*g*-PAMAM-AO

The target product Fe_3O_4@SiO_2-*g*-G2.0 microspheres were dispersed in a solution of glutaraldehyde and ethanol. The mixture was reacted and stirred continuously at 30 °C for 3 h. Then, the particles reacted with glutaraldehyde in an aqueous solution of 4-aminobenzonitrile and ethanol. The black solid was washed and separated after 3 h at 30 °C, and then K_2CO_3 and NH_2OH HCl were added into an aqueous solution of distilled water and ethanol to react at 80 °C in a three-necked flask. The final Fe_3O_4@SiO_2-*g*-PAMAM-AO product was obtained. A schematic presentation of the synthesis process is shown in Fig. 1.

2.5 Characterization of Fe_3O_4@SiO_2-*g*-PAMAM-AO nanohybrids

The morphology and elemental distribution of the nanoparticles were characterized by transmission electron microscopy (TEM), energy-dispersive spectroscopy (EDS), and scanning electron microscopy (SEM). The X-ray diffraction (XRD) patterns of Fe_3O_4@SiO_2-*g*-PAMAM-AO were recorded by a Philips X'Pert Pro Super X-ray diffractometer with a Cu Kα source (k = 1.54178 Å). Fourier transformed infrared (FT-IR) spectra were recorded on a Nicolet Magna-IR 750 spectrometer with KBr pellets at room temperature.

2.6 Adsorption experiments

$Pb(NO_3)_2$ and $Ni(NO_3)_2 \cdot 6H_2O$ were dissolved in distilled water to prepare the solution of Pb^{2+} and Ni^{2+}. For the adsorption isotherm and adsorption thermodynamic experiments with

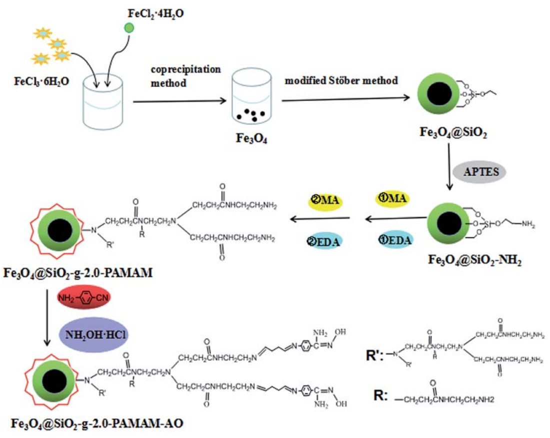

Fig. 1 A schematic presentation of the synthesis process.

Pb^{2+} and Ni^{2+}, 25 mg of $Fe_3O_4@SiO_2$-*g*-PAMAM-AO were respectively added into solutions of different concentrations, which were 50, 100, 150, 200, 225,250, 275 and 300 mg L^{-1}. And then the mixture was reacted at 25 °C, 35 °C and 45 °C for 2 h. The above solutions were separated by a magnet and then analyzed by an atomic absorption spectrometer (AAS, AA-6800). To study the effect of pH on the adsorption reaction, 25 mg of $Fe_3O_4@SiO_2$-*g*-PAMAM-AO was reacted with 50 ml of ionic solution (50 mg L^{-1}) at 25 °C for 2 h. 0.1 mol L^{-1} HNO_3 and 0.1 mol L^{-1} NaOH were added to adjust the pH. In addition, to study the effect of contact time, the time ranged from 5 to 180 minutes. The Pb^{2+} and Ni^{2+} percentage removals (adsorption efficiency) were determined using eqn (1):[23]

$$R(\%) = \frac{(C_0 - C_e)}{C_0} \times 100\% \tag{1}$$

where C_0 and C_e (mg L^{-1}) are the initial Pb^{2+} and Ni^{2+} concentrations and the equilibrium Pb^{2+} and Ni^{2+} concentrations, respectively.

The equilibrium sorption capacity was determined using eqn (2):[24]

$$q_e = \frac{(C_0 - C_e)V}{m} \tag{2}$$

where q_e is the equilibrium amount of Pb^{2+} and Ni^{2+} adsorbed per unit mass of adsorbent (mg g^{-1}) and V is the sample volume (L). All experimental data were determined by repeated experiments.

2.7 Desorption experiment

To test the reusability and regenerability of $Fe_3O_4@SiO_2$-*g*-PAMAM-AO, 25 mg of $Fe_3O_4@SiO_2$-*g*-PAMAM-AO was respectively added into solutions of Pb(II) and Ni(II) (50 ml, 50 mg L^{-1}). Then using NaOH to adjust the pH, the pH of Pb(II) and Ni(II) were 5.5 and 8.0, respectively. The desorption experiment was reacted at 30 °C for 2 h. After desorption, the mixture was collected in a conical flask. The $Fe_3O_4@SiO_2$-*g*-PAMAM-AO was washed with HNO_3 and distilled water until the solution reached a pH of 7. To test the reusability of $Fe_3O_4@SiO_2$-*g*-PAMAM-AO, this was repeated using five-consecutive adsorption–desorption cycles.

3. Results and discussion

3.1 Characterization

Fig. 2 shows the FT-IR spectra of Fe_3O_4 (a), $Fe_3O_4@SiO_2$ (b), $Fe_3O_4@SiO_2$-*g*-G2.0 (c), $Fe_3O_4@SiO_2$-*g*-PAMAM (d) and $Fe_3O_4@SiO_2$-*g*-PAMAM-AO (e). The vibrating characterization at 575 cm^{-1} was associated with the Fe–O stretching vibration (Fig. 2a). Two peaks of 1049 cm^{-1} and 1091 cm^{-1} are relevant to the stretching vibration of Si–O–Si, and the absorption peak at 463 cm^{-1} corresponds to the O–Si–O bending vibration. All the evidence indicated that silica was successfully coated onto the surface of Fe_3O_4. In the spectrum of $Fe_3O_4@SiO_2$ (Fig. 2b), the absorption peak at 3424 cm^{-1} is attributed to the H–O stretching vibration. A broad and strong peak at 3430 cm^{-1} is related to the O–H stretching vibration. In addition, the peak at 3430 cm^{-1} is related to the N–H stretching vibration of the $-NH_2$ groups. The peak at 2970 cm^{-1} corresponds to the $-CH_2$ asymmetric stretching vibration. The characteristic band at 1641 cm^{-1} is attributed to the secondary amide stretching of C=O, which indicated the existence of the acylamino group (–NHCO–) in PAMAM (Fig. 2c). The peaks observed at 1558 cm^{-1} and 1552 cm^{-1} are ascribed to the C=C stretching vibrations of benzene. After modification with 4-aminobenzonitrile, the existence of new peaks at 2365 cm^{-1} and 2344 cm^{-1} is related to the stretching vibration of C≡N (Fig. 2d). The disappearance of the absorption bands of C≡N and the appearance of two new bands at 1640 cm^{-1} and 954 cm^{-1} are explained well by the C=N and N–O stretching vibrations of the amidoxime groups, respectively (Fig. 2e).

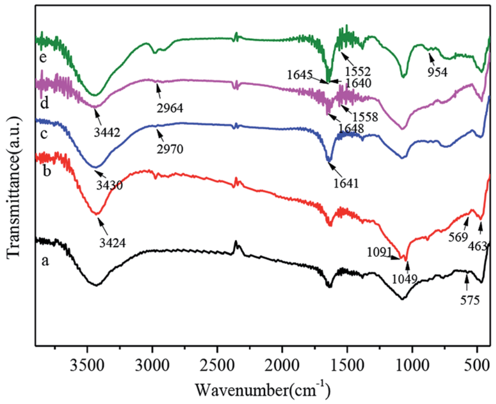

Fig. 2 FT-IR spectra of Fe_3O_4 (a), $Fe_3O_4@SiO_2$ (b), $Fe_3O_4@SiO_2$-*g*-G2.0 (c), $Fe_3O_4@SiO_2$-*g*-PAMAM (d), $Fe_3O_4@SiO_2$-*g*-PAMAM-AO (e).

Fig. 3 shows the XRD patterns of Fe_3O_4 (a), $Fe_3O_4@SiO_2$ (b), $Fe_3O_4@SiO_2–NH_2$ (c) and $Fe_3O_4@SiO_2$-*g*-PAMAM-AO (d). In Fig. 3a, the diffraction peaks in curve a at the bands (220), (311), (400), (422), (511) and (440) can be indexed as characteristic of Fe_3O_4 with a face-centered cubic (fcc) phase (JCPDS no. 75-0033).[25] After coating with the silica layer, the diffraction peaks in curve b at 20–30° were observed, confirming the formation of silica. Moreover, the diffraction peaks of Fe_3O_4 in Fig. 3b–d are very similar to Fig. 3a, indicating that the Fe_3O_4 crystal structure did not change during the process of APTES and grafting by PAMAM.

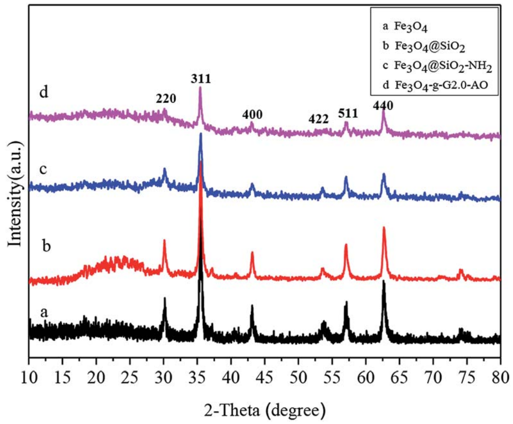

Fig. 3 The XRD pattern of Fe_3O_4 (a), $Fe_3O_4@SiO_2$ (b), $Fe_3O_4@SiO_2–NH_2$ (c), $Fe_3O_4@SiO_2$-*g*-PAMAM-AO (d).

To better analyze the electronic structure and chemical composition, a fine-scan XPS of Fe_3O_4@SiO_2-*g*-PAMAM-AO was performed. The high-resolution deconvoluted C 1s spectrum in Fig. 4a confirmed three different peaks at 284.6, 285.9 and 288.0 eV, respectively, representing the typical XPS characteristics of Fe_3O_4@SiO_2-*g*-PAMAM-AO. The binding energy peak at 284.6 eV is ascribed to the removal of the oxygen groups' carbon component of C–C (sp^2-hybridized); the peaks at 285.9, 288.0 eV represent C–O bonding, and O=C–N bonding, respectively. The bonding of –NHCO– is also indicative of the successful combination between the –COOH groups and the $-NH_2$ groups, demonstrating that PAMAM underwent a successful grafting reaction on the Fe_3O_4 surface. The high-resolution spectrum of Fe 2p shown in Fig. 4b can be deconvoluted into two obviously different peaks at 724.4 and 711.2 eV, corresponding to Fe $2p_{1/2}$ and Fe $2p_{3/2}$, respectively, which are in accordance with the reported values for Fe_3O_4 (ref. 26 and 27). As shown in Fig. 4c, the binding energy peak appearing at 398.2 eV is ascribed to the quinoid imine (=N–) for Fe_3O_4@SiO_2-*g*-G2.0-AO. The binding energy peaks appearing at 398.8 eV and 399.7 eV are related to –NH– and $-NH_2$, respectively. The fine-scan XPS spectrum (Fig. 4d) of Fe_3O_4@SiO_2-*g*-G2.0-AO illustrates that Fe_3O_4@SiO_2-*g*-PAMAM-AO includes Fe, N, O, Si and C elements.

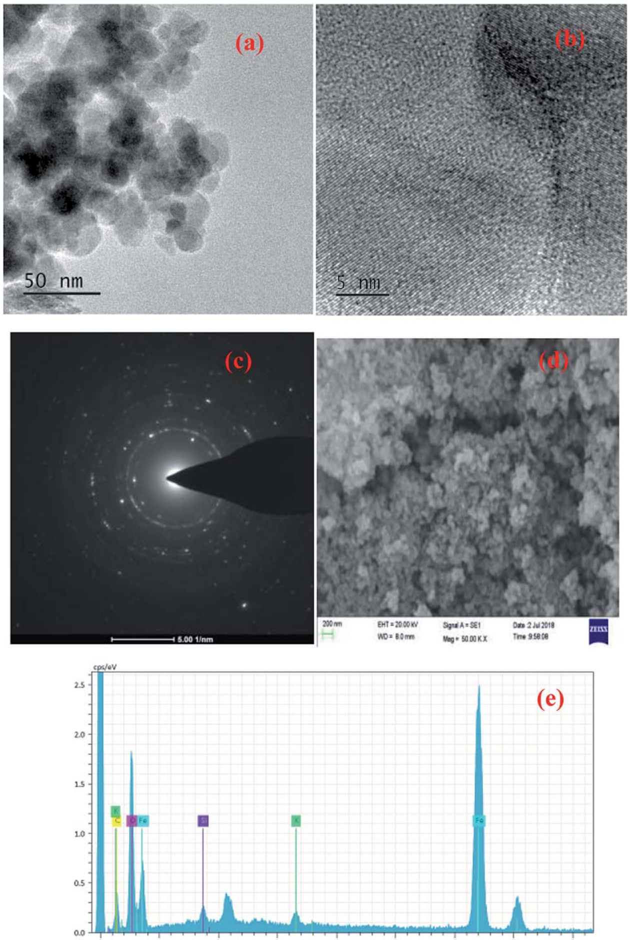

Fig. 5 The TEM of (a) sample Fe_3O_4@SiO_2-*g*-PAMAM-AO and the HRTEM image of (b) sample Fe_3O_4@SiO_2-*g*-PAMAM-AO and the SAED pattern of (c) sample Fe_3O_4@SiO_2-*g*-PAMAM-AO and the SEM of (d) sample Fe_3O_4@SiO_2-*g*-PAMAM-AO and the EDS of (e).

Fig. 5 shows the TEM, SEM, SAED and EDS images of Fe_3O_4@SiO_2-*g*-PAMAM-AO. From Fig. 5a, we can see that Fe_3O_4@SiO_2-*g*-PAMAM-AO has an obvious core–shell structure with a core of about 25 nm and a shell of about 10 nm. The HRTEM image (Fig. 5b) shows well-resolved lattice fringes with an interplane distance of 0.417 nm. The SAED pattern (Fig. 5c) shows that Fe_3O_4@SiO_2-*g*-PAMAM-AO is polycrystalline in nature, confirming that the nanoparticles have the magnetic cubic structure of the Fe_3O_4 phase and consist of small nanocrystals. As can be seen from the SEM image (Fig. 5d), this product contains more sphere-like shapes and has a narrower size distribution. The EDS image (Fig. 5e) of Fe_3O_4@SiO_2-*g*-PAMAM-AO suggests that Fe is the major constituent of Fe_3O_4@SiO_2-*g*-PAMAM-AO. Other elements are oxygen, carbon, silicon and potassium.

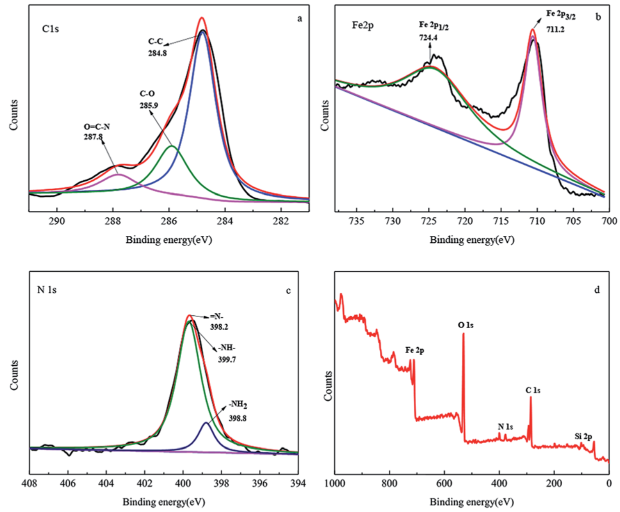

Fig. 4 The high-resolution scan XPS spectra of C 1s (a), Fe 2p (b), N 1s (c), and the survey scan XPS spectra (d) of Fe_3O_4@SiO_2-*g*-PAMAM-AO.

The TGA curve and DSC curve are shown in Fig. 6. In the TGA curve of Fe_3O_4@SiO_2-*g*-PAMAM-AO (Fig. 6a), the weight loss is divided into two distinct sections. In the first section, between

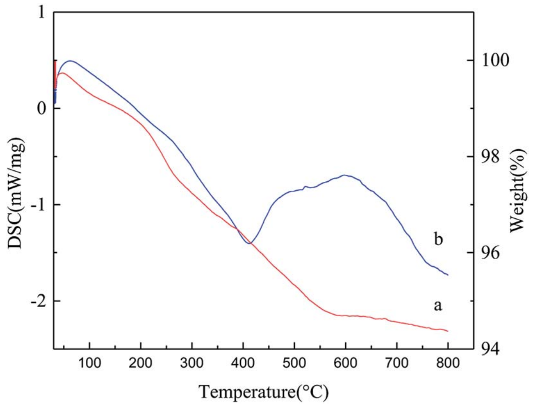

Fig. 6 Thermogravimetric analysis (TGA) curve (a) and differential scanning calorimetry (DSC) curve (b) of Fe_3O_4@SiO_2-*g*-PAMAM-AO.

32 °C and 200 °C, the weight loss of 1.08% is ascribed to the loss of bound water adsorbed on the microspheres. The second section of weight loss (close to 3.95%), at temperatures from 200 °C to 580 °C, was also indicative of the thermal decomposition of the surface amidoxime groups. The DSC curves recorded during the endothermic and exothermic processes of Fe_3O_4@SiO_2-*g*-PAMAM-AO are shown in Fig. 6b. The first endothermic peak is less than 400 °C, accompanied by a significant mass loss on the TGA curve, which can be attributed to the oxidation of carbon on the silicon surface. The second endothermic peak between 400 °C and 700 °C was largely related to the pyrolysis of organic molecules on the shell surface.

The N_2 adsorption and desorption isotherm of Fe_3O_4@SiO_2-*g*-PAMAM-AO is demonstrated in Fig. 7. From the BET results, the isotherm of Fe_3O_4@SiO_2-*g*-PAMAM-AO accords with the IV adsorption isotherm, which illustrates that Fe_3O_4@SiO_2-*g*-PAMAM-AO is a mesoporous structure. Furthermore, it is clear that the surface area is 73.493 $m^2\ g^{-1}$. This illustrates that Fe_3O_4@SiO_2-*g*-PAMAM-AO has a large surface area.

Fig. 8 depicts the magnetization hysteresis loop of Fe_3O_4@SiO_2-*g*-PAMAM-AO at room temperature. The saturation magnetization (SM) value of the Fe_3O_4@SiO_2-*g*-PAMAM-AO nanoparticles is 47.7 emu g^{-1}. It is worth noting that the nanoparticles have no obvious coercivity and remanence in the magnetization curves, illustrating that Fe_3O_4@SiO_2-*g*-PAMAM-AO possesses superparamagnetism. As shown in the inset of Fig. 8, Fe_3O_4@SiO_2-*g*-PAMAM-AO nanoparticles were uniformly dispersed in aqueous solution, which was then placed in an external non-magnetic field. Because Fe_3O_4@SiO_2-*g*-PAMAM-AO has strong ferromagnetic behavior, an external magnet can make the absorbed contaminant easily separable from the solution.

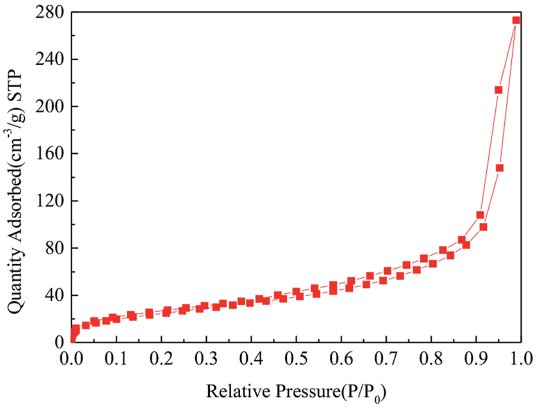

Fig. 7 N_2 adsorption and desorption isotherm of Fe_3O_4@SiO_2-*g*-PAMAM-AO.

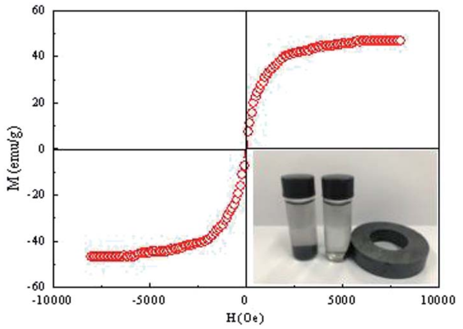

Fig. 8 Magnetization curve of Fe_3O_4@SiO_2-*g*-PAMAM-AO; the inset shows a photograph of Fe_3O_4@SiO_2-*g*-PAMAM-AO dispersion in ethanol and its magnetic response when placed in an external magnetic field (right).

3.2 Adsorption studies

3.2.1 Effect of pH. The effect of pH is a key factor in determining the adsorption performance for Pb(II) and Ni(II) in aqueous solutions. As shown in Fig. 9, with the pH increasing from 2.0 to 3.0, the adsorption capacity for Pb(II) increased slowly. However, with the pH increasing from 3.0 to 5.5, the adsorption ability for Pb(II) increased enormously. As shown in the inset of Fig. 9, in the pH range 6.0–7.0, the adsorption ability of Pb(II) reached a plateau. Because of the pH range from 6.0 to 7.0, a white sediment appeared in the aqueous solution. For the adsorption of Ni(II), adsorption experiments were investigated in the pH range between 2.0 and 9.0. It can be seen from Fig. 8 that the adsorption capacity for Ni(II) increased enormously from 2.0 to 8.0, then reached a maximum value with the pH reaching 8.0–9.0. Comparing the adsorption performances for Pb(II) and Ni(II), Fe_3O_4@SiO_2-*g*-PAMAM-AO has higher adsorption ability for Ni(II) all over the ranges of pH. The relative distribution of Pb(II) in the aqueous solution and the surface properties of Fe_3O_4@SiO_2-*g*-PAMAM-AO can be affected by the pH. For the adsorption of Pb^{2+} and Ni^{2+}, the amidoxime group can have a bidentate ligand effect. The lone pairs of electrons on the amino nitrogen and the oxime oxygen induced the positive Pb(II) and Ni(II) centers to construct a new five-membered ring including the metal ion. It is worth noting that the oxime oxygen can undergo metal-assisted deprotonation:

$$R\text{–}C(NH_2)N\text{–}OH \leftrightarrow R\text{–}C(NH_2)N\text{–}O^- + H^+ \tag{3}$$

$$2R\text{–}C(NH_2)N\text{–}O^- + Pb^{2+} \leftrightarrow Pb(R\text{–}C(NH_2)N\text{–}O)_2 \tag{4}$$

$$2R\text{–}C(NH_2)N\text{–}O^- + Ni^{2+} \leftrightarrow Ni(R\text{–}C(NH_2)N\text{–}O)_2 \tag{5}$$

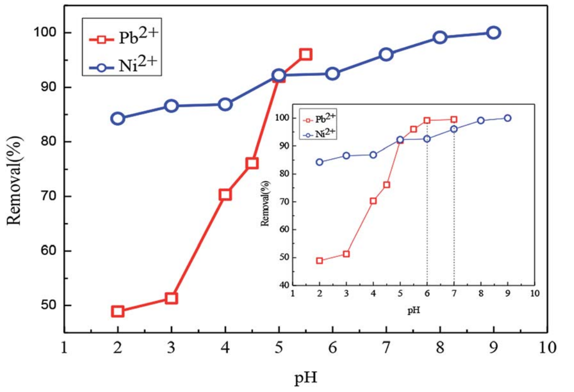

Fig. 9 Effect of pH on the adsorption of Fe_3O_4@SiO_2-*g*-PAMAM-AO for Pb(II) and Ni(II) (Co = 50 mg L^{-1}, T = 298 K, t = 2 h).

With the pH increasing, the emitted H^+ ions can be neutralized under the chelation reaction environment. When the functional groups were deprotonated, the repulsion between Pb^{2+}/Ni^{2+} and Fe_3O_4@SiO_2-*g*-PAMAM-AO decreased. Therefore, the sorption amounts of the samples for Pb(II) and Ni(II) were increased. The main reason is ascribed to the fact that amidoxime chelating functional groups on the surfaces of Fe_3O_4@SiO_2-*g*-PAMAM-AO can construct stable chelates with Pb(II) and Ni(II).

3.2.2 Effect of contact time and adsorption kinetics. Then we employed the nanoparticles Fe_3O_4@SiO_2-*g*-PAMAM-AO as adsorbents to investigate the impact of contact time on the removal of Pb(II) and Ni(II). As shown in Fig. 10, the adsorption ability increased slowly. However, the adsorption ability of Fe_3O_4@SiO_2-*g*-PAMAM-AO for Pb(II) and Ni(II) approaches equilibrium after 10 min. As shown in Fig. 10, the adsorption ability of Fe_3O_4@SiO_2-*g*-PAMAM-AO for Ni(II) is higher than for Pb(II) under the same conditions ($Co = 50$ mg L^{-1}, $T = 298$ K, $t = 180$ min).

To gain further insight into the adsorption kinetics, the pseudo-first-order equation and pseudo-second-order equation were adopted to explain the adsorption mechanism. The pseudo-first-order and pseudo-second-order equations are defined as eqn (6) and (7),[28,29] respectively.

$$\ln(Q_e - Q_t) = \ln Q_e - k_1 t \tag{6}$$

$$\frac{t}{Q_t} = \frac{1}{k_2 {Q_e}^2} + \left(\frac{1}{Q_e}\right) t \tag{7}$$

where Q_e (mg g^{-1}) and Q_t (mg g^{-1}) are the Pb(II) and Ni(II) adsorption capacities at equilibrium, respectively, t (min) is the constant time, k_1 (min^{-1}) and k_2 (g mg^{-1} min^{-1}) are the pseudo-first-order and pseudo-second-order rate constants, respectively.

Fig. 11 and Table 1 provide more intuitive depictions of the statistical results. From the values of the correlation coefficients, Pb(II) and Ni(II) adsorptions are more consistent with the pseudo-second-order model in comparison with the pseudo-first-order model. The results indicated that the chemical adsorption is the main adsorption mechanism of Fe_3O_4@SiO_2-*g*-PAMAM-AO for Pb(II) and Ni(II).

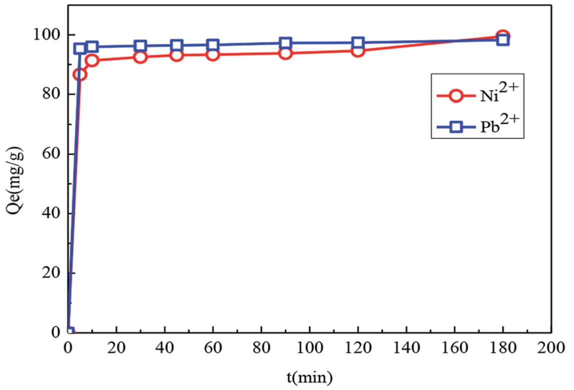

Fig. 10 The effect of contact time on the adsorption of Fe_3O_4@SiO_2-*g*-PAMAM-AO for Pb(II) ($Co = 50$ mg L^{-1}, $T = 298$ K, pH = 5.5) and Ni(II) ($Co = 50$ mg L^{-1}, $T = 298$ K, pH = 8).

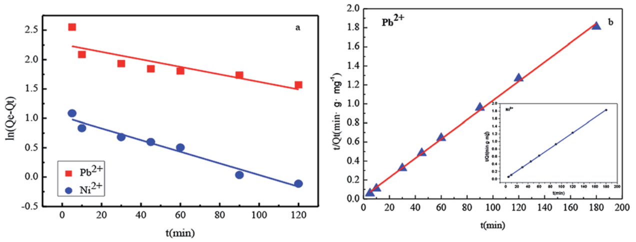

Fig. 11 Pseudo-first-order (a) and pseudo-second-order (b) kinetics of Pb(II) and Ni(II) adsorption on Fe_3O_4@SiO_2-*g*-PAMAM-AO. ($Co = 50$ mg L^{-1}, $T = 298$ K, pH(Pb^{2+}) = 5.5, pH(Ni^{2+}) = 8).

Table 1 The parameters of the kinetics of Pb^{2+} and Ni^{2+} adsorption onto Fe_3O_4@SiO_2-*g*-PAMAM-AO

Model	Parameter	Pb^{2+}	Ni^{2+}
Pseudo-first-order model	Q_e (mg g^{-1})	10.3605	4.0678
	k_1	0.0064	0.0099
	R^2	0.7272	0.9631
Pseudo-second-order model	Q_e (mg g^{-1})	49.0294	49.143
	k_2	0.01012	0.01018
	R^2	0.99843	0.99994

3.2.3 Adsorption isotherm. In order to illustrate the adsorption mechanism of Fe_3O_4@SiO_2-*g*-PAMAM-AO, the interaction between adsorbent and adsorbate was studied. The adsorption data were analyzed according to the well-known Langmuir and Freundlich isotherm models, whose equations are respectively expressed by eqn (8) and (9).[30,31]

$$\frac{C_e}{Q_e} = \left(\frac{1}{Q_{max}}\right) C_e + \frac{1}{k_L Q_{max}} \tag{8}$$

$$\log Q_e = \log k_F + \frac{1}{n} \log C_e \tag{9}$$

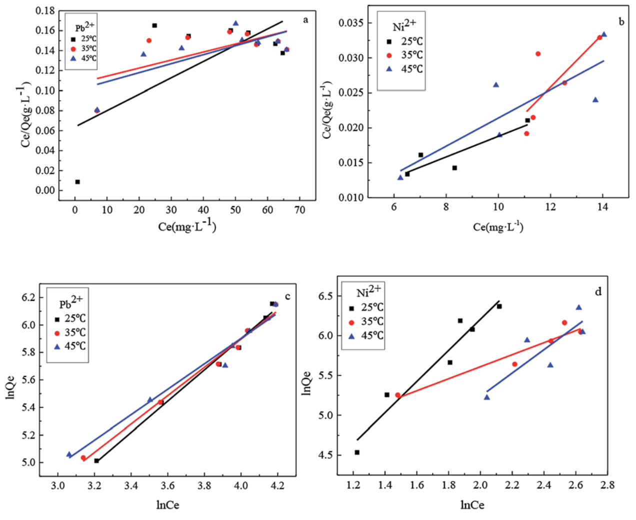

Fig. 12 The Langmuir (a), (b) and Freundlich (c), (d) isotherms of Pb(II) and Ni(II) adsorption onto Fe_3O_4@SiO_2-*g*-PAMAM-AO.

Table 2 Langmuir and Freundlich isotherm parameters for Pb^{2+} and Ni^{2+} adsorption onto the $Fe_3O_4@SiO_2$-*g*-PAMAM-AO nanocomposite

Heavy metal ions	Temperature (°C)	Langmuir model			Freundlich model		
		k_L	Q_e (mg g^{-1})	R^2	k_F	N	R^2
Pb^{2+}	25	0.023	150.3588	0.6913	118.15	13.895	0.9946
	35	0.021	153.846	0.6506	121.78	8.876	0.9950
	45	0.017	157.2578	0.7475	133.25	6.729	0.9881
Ni^{2+}	25	0.026	191.7856	0.8864	137.46	15.138	0.9678
	35	0.024	191.2116	0.7538	125.18	11.257	0.9576
	45	0.019	184.6080	0.8409	123.29	7.623	0.8493

Table 3 Comparison of adsorption capacity of $Fe_3O_4@SiO_2$-*g*-PAMAM-AO composite nanoparticle adsorbent with other nanoparticles adsorbents

Adsorbent	Adsorbate	Adsorption capacity	References
Fe_2O_3–Al_2O_3	Pb^{2+}	23.75 (mg g^{-1})	29
Magnetic Fe_3O_4 yeast treated with EDTA dianhydride	Pb^{2+}	99.26 (mg g^{-1})	30
Chain-like $Fe_3O_4@SiO_2$@chitosan magnetic nanoparticles	Pb^{2+}	6.899 (μg mg^{-1})	31
Magnetic multiwalled carbon nanotube nanocomposite	Ni^{2+}	2.11 (mg g^{-1})	32
Iron oxide nanoparticles	Ni^{2+}	11.1 (mg g^{-1})	33
$Fe_3O_4@SiO_2$-*g*-PAMAM-AO magnetic nanoparticles	Pb^{2+}	157.25 (mg g^{-1})	This work
	Ni^{2+}	191.78 (mg g^{-1})	This work

where Q_e, Q_{max} (mg g^{-1}) are the equilibrium adsorption capacity and the maximum adsorption capacity of Pb(II) and Ni(II) on the adsorbent, respectively. C_e (mg L^{-1}) is the Pb(II) and Ni(II) concentration residual in solution at equilibrium, K_L (L mg^{-1}) is the Langmuir adsorption constant, and K_F and n are the Freundlich constants related to the adsorption capacity and the adsorption intensity, respectively.

As shown in Fig. 12, it can be observed that the adsorption isotherms of Pb(II) and Ni(II) could be fitted with both Langmuir (a), (b) and Freundlich (c), (d) models. The parameters calculated by the model are listed in the support information to Table 2. For the adsorption isotherms of Pb(II) and Ni(II), the Freundlich model showed a higher correlation coefficient, indicating that the adsorption data of the Freundlich model is a better fit than the adsorption data of the Langmuir model. Therefore, the Freundlich isotherm can be applied for non-ideal adsorption on multilayer adsorption and heterogeneous surfaces in nature.[32]

Compared with other magnetic adsorbents, the adsorption capacities on $Fe_3O_4@SiO_2$-*g*-PAMAM-AO for Pb(II) and Ni(II) are higher than those for Pb(II) and Ni(II) sorption on other related materials, as listed in Table 3. $Fe_3O_4@SiO_2$-*g*-PAMAM-AO with such a high ability for Pb(II) and Ni(II) sorption exhibits a potential for real applications in the removal of Pb(II) and Ni(II) from large volumes of aqueous solutions. The main reason for the high adsorption capacity is that the dendritic graftings have a large surface area. Furthermore, the amidoxime-functionalized groups have multivariate coordination characteristics.

Fig. 13 shows the effects of adsorbent dose on the removal efficiency of Pb(II) and Ni(II) in aqueous solution. For Pb(II), when the adsorbent dose increased from 0 to 30 mg, the removal efficiency quickly increased from 0 to 96%. For Ni(II), the removal efficiency rapidly increased from 0 to 99.1% with the adsorbent dose under the same conditions. Because an increase in the adsorbent dose meant an improvement, there are relatively more active sites and greater surface area.

The regeneration and reuse of adsorbent materials play a decisive role in practical applications.[33–37] In this work, the Pb(II)-loaded adsorbent was desorbed using a 0.1 mol L^{-1} NaOH solution and then washed with distilled water to a pH of 7.0 for reuse in the next run. For Pb(II), it was found that the removal efficiency was approximately 93.74%, and the removal capacity was still over 91.256% after five adsorption–desorption cycles. Furthermore, for Ni(II), it was found that the

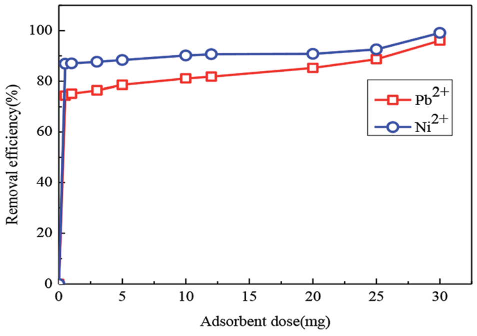

Fig. 13 Effect of adsorbent dose on the removal efficiency of Pb(II) and Ni(II) by $Fe_3O_4@SiO_2$-*g*-PAMAM-AO. (Co = 50 mg L^{-1}, T = 298 K, pH (Pb^{2+}) = 5.5, pH (Ni^{2+}) = 8, t = 2 h).

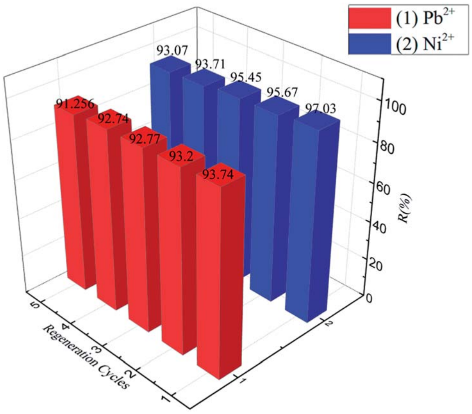

Fig. 14 Removal efficiency of five adsorption–desorption cycles of regenerating Fe_3O_4@SiO_2-*g*-PAMAM-AO on Pb(II) and Ni(II). (C_o = 50 mg L^{-1}, T = 298 K, pH (Pb^{2+}) = 5.5, pH (Ni^{2+}) = 8, t = 2 h).

removal efficiency was approximately 97.03%, and the removal capacity was still over 93.07% after five adsorption–desorption cycles (Fig. 14). These results indicated that Fe_3O_4@SiO_2-*g*-PAMAM-AO has good ability of regeneration, and it can be reused in the application of Pb(II) and Ni(II) removal from wastewater.

4. Conclusions

In summary, magnetic Fe_3O_4@SiO_2-*g*-PAMAM-AO was successfully synthesized and used as an adsorbent for the adsorption of Pb(II) and Ni(II) from several environmental waters. Fe_3O_4@SiO_2-*g*-PAMAM-AO exhibits enhanced adsorption capacities for both Pb(II) and Ni(II) because of the larger surface area and the strong chelation of amidoxime to Pb(II) and Ni(II). The adsorption process was pH dependent. FT-IR and XPS studies revealed the amidoxime-functionalized groups formed on the Fe_3O_4@SiO_2-*g*-PAMAM-AO. Magnetic measurement revealed the superparamagnetic behavior of Fe_3O_4@SiO_2-*g*-PAMAM-AO with a saturation magnetization of 47.7 emu g^{-1}. The adsorption processes of Fe_3O_4@SiO_2-*g*-PAMAM-AO for Pb(II) and Ni(II) were in good agreement with the pseudo-second-order kinetics model and the Freundlich isotherm model. Fe_3O_4@SiO_2-*g*-PAMAM-AO has a maximum Pb(II) adsorption of 157.25 mg g^{-1}(100 mg L^{-1}) at pH 5.5. Furthermore, Fe_3O_4@SiO_2-*g*-PAMAM-AO showed an excellent adsorption performance for the removal of Ni(II) with a maximum adsorption capacity of 191.78 mg g^{-1} (100 mg L^{-1}) at pH 8.0. The adsorption capacities of Fe_3O_4@SiO_2-*g*-PAMAM-AO nanohybrids grafted with amidoxime-functionalized groups for Pb(II) and Ni(II) are very high. All the results suggested that the Fe_3O_4@SiO_2-*g*-PAMAM-AO composites are effective adsorbents for the removal of Pb(II) and Ni(II).

Conflicts of interest

There are no conflicts to declare.

Acknowledgements

The authors greatly acknowledge the financial support provided by the National Natural Science Foundation of China (21671026), the Natural Science Foundation of Hunan Province (2019JJ40310), the Science and Technology Key Project of Hunan Province (2015SK20823), Scientific Research Key Fund of Hunan Provincial Education Department (15A001).

Notes and references

1 Y. G. Zhao, H. Y. Shen, S. D. Pan, M. Q. Hu and Q. H. Xia, *J. Mater. Sci.*, 2010, **45**, 5291–5301.
2 N. H. Rashidi, I. W. Wan, I. Ali and M. M. Sanagi, *Environ. Sci. Pollut. Res.*, 2016, **23**, 9759–9773.
3 Y. Dai, L. Niu, J. Zou, T. Chen, H. Liu and Y. Zhou, *Chin. Chem. Lett.*, 2018, **29**, 887–891.
4 W. Hou, X. Yuan, W. Yan, X. Chen, L. Leng and W. Hui, *Chem. Eng. J.*, 2015, **262**, 597–606.
5 G. Liu, Q. Deng, H. Wang, S. Kang, Y. Yang and D. H. Ning, *Chem.–Eur. J.*, 2012, **18**, 13418–13426.
6 J. H. Wang, S. R. Zheng, Y. Shao, J. L. Liu, Z. Y. Xu and D. Q. Zhu, *J. Colloid Interface Sci.*, 2010, **349**, 293–299.
7 X. Sun, L. Yang, H. Xing, J. Zhao, X. Li and Y. Huang, *Chem. Eng. J.*, 2013, **234**, 338–345.
8 V. Chandra, J. Park, Y. Chun, J. W. Lee, I. C. Huang and K. S. Kim, *ACS Nano*, 2010, **4**, 3979–3986.
9 H. Shi, J. Yang, L. Zhu, Y. Yang, H. Yuan and Y. Yang, *J. Nanosci. Nanotechnol.*, 2016, **16**, 1871–1882.
10 Z. Fan, Y. Shi, Z. Zhao, B. Ma, L. Wei and L. Lu, *J. Mater. Sci.*, 2014, **49**, 3478–3483.
11 Y. Li, L. Cao, L. Li and C. Yang, *J. Hazard. Mater.*, 2015, **289**, 140–148.
12 N. H. Shaidan, U. Eldemerdash and S. Awad, *J. Taiwan Inst. Chem. Eng.*, 2012, **43**, 40–45.
13 L. A. Wei, A. W. Mohammad, N. Hilal and C. P. Leo, *Desalination*, 2015, **363**, 2–18.
14 I. Mobasherpour, M. S. Heshajin, A. Kazemzadeh and M. Zakeri, *J. Alloys Compd.*, 2007, **430**, 330–333.
15 R. Donat, A. Akdogan, E. Erdem and H. Cetisli, *J. Colloid Interface Sci.*, 2005, **286**, 43–52.
16 Y. Zhao, J. Li, L. Zhao, S. Zhang, Y. Huang and X. Wu, *Chem. Eng. J.*, 2014, **235**, 275–283.
17 N. Lu, M. Zhang, L. Ding, J. Zheng, C. X. Zeng, Y. L. Wen and G. Liu, *Nanoscale*, 2017, **9**, 4508–4515.
18 J. P. Wang, M. Zhang, J. L. Xu and J. Zheng, *Dalton Trans.*, 2018, **47**, 2791–2798.
19 Y. X. Ma, Y. L. Kou, D. Xing, P. S. Jin, W. J. Shao and X. Li, *J. Hazard. Mater.*, 2017, **340**, 407–416.
20 P. Zhao, L. Tian, X. Li, Z. Ali, B. Zhang and H. Zhang, *ACS Sustainable Chem. Eng.*, 2016, **4**, 1–28.
21 M. Anbarasu, M. Anandan, E. Chinnasamy, V. Gopinath and K. Balamurugan, *Spectrochim. Acta, Part A*, 2015, **135**, 536–539.
22 Y. Kobayashi, H. Katakami, E. Mine, D. Nagao, M. Konno and L. M. Lizmarzán, *J. Colloid Interface Sci.*, 2005, **283**, 392–396.

23 K. Zhu, Y. Duan, F. Wang, P. Gao, H. Jia and C. Ma, *Chem. Eng. J.*, 2017, **311**, 236–246.
24 Q. Peng, M. Liu, J. Zheng and C. Zhou, *Microporous Mesoporous Mater.*, 2015, **201**, 190–201.
25 J. Mu, B. Chen, Z. Guo, M. Zhang, Z. Zhang and P. Zhang, *Nanoscale*, 2011, **3**, 5034–5040.
26 A. B. Albadarin, M. N. Collins, M. Naushad, S. Shirazian, G. Walker and C. Mangwandi, *Chem. Eng. J.*, 2017, **307**, 264–272.
27 M. Zhang, L. F. Chen, J. Zheng and W. Z. Li, *Dalton Trans.*, 2017, **46**, 9172–9179.
28 J. P. Simonin, *Chem. Eng. J.*, 2016, **300**, 254–263.
29 V. P. Mahida and M. P. Patel, *RSC Adv.*, 2016, **6**, 21577.
30 K. Y. Foo and B. H. Hameed, *Chem. Eng. J.*, 2010, **156**, 2–10.
31 B. S. Kaith, R. Jindal and R. Sharma, *RSC Adv.*, 2015, **5**, 43092.
32 Z. Wang, S. Zhu, S. Zhao and H. Hu, *J. Alloys Compd.*, 2011, **509**, 6893–6898.
33 A. R. Keshtkar, M. Irani and M. A. Mousavian, *J. Radioanal. Nucl. Chem.*, 2013, **295**, 563–571.
34 X. Meng, Y. Zhang, Z. Zhang, Y. Shen, M. Zhao and G. Pan, *Chem. Eng. J.*, 2011, **168**, 737–745.
35 H. Shi, J. Yang, L. Zhu, Y. Yang, H. Yuan, Y. Yang and X. Liu, *J. Nanosci. Nanotechnol.*, 2016, **16**, 1871–1882.
36 W. Konicki, I. Pełech and E. Mijowska, *Pol. J. Chem. Technol.*, 2014, **16**, 87–94.
37 S. E. Ebrahim, A. H. Sulaymon and H. S. Alhares, *Desalin. Water Treat.*, 2015, **62**, 1–15.